Title
Design and Performance Analysis for a Sulfur-based Thermal Energy Storage System using Intermodal Containment

Author
Shinn, Mitchell Anthony

Publication Date
2016

Peer reviewed|Thesis/dissertation

UNIVERSITY OF CALIFORNIA

Los Angeles

Design and Performance Analysis for a Sulfur-based Thermal Energy Storage System using Intermodal Containment

A thesis submitted in partial satisfaction

of the requirements for the degree

Master of Science in Mechanical Engineering

by

Mitchell Anthony Shinn

2016

ABSTRACT OF THE THESIS

Design and Performance Analysis for a Sulfur-based Thermal Energy Storage System using Intermodal Containment

by

Mitchell Anthony Shinn

Master of Science in Mechanical Engineering

University of California, Los Angeles, 2016

Professor Richard E. Wirz, Chair

Currently, intermittent energy sources can be coupled to thermal energy storage (TES) systems in order to store excess energy so that it can later be dispatched for times of high energy demand. Elemental sulfur is a promising candidate storage fluid for high temperature TES systems due to its high energy density, moderate vapor pressure, high thermal stability, and low cost. The objective of this effort is to use a transient, two-dimensional numerical model to investigate the design and performance of a thermal energy storage (TES) system that uses sulfur stored isochorically in an intermodal shell

and tube thermal battery configuration. Parametric studies are conducted to determine the effect of design and operating parameters on the overall utilization of energy stored within the system, exergetic efficiency, and weld length per utilized capacity.

The study shows that there is a preferred tube diameter based on the competing effects of exergetic efficiency – which should be maximized – and total weld length of tubes in a system – which should be minimized. Based on the systematic parametric studies, recommendations on the design of an elemental sulfur based TES system using standard intermodal containment shell geometry are made.

The thesis of Mitchell Anthony Shinn is approved.

H. Pirouz Kavehpour

Adrienne S. Lavine

Richard E. Wirz, Committee Chair

University of California, Los Angeles

2016

ACKNOWLEDGMENTS

I would like to thank Professor Wirz for giving me the opportunity to work on such an important and interesting research topic as well as his guidance during my time at UCLA. I also would like to thank Dr. Karthik Nithyanandam for his guidance in creating the numerical model described in this thesis, as well as Dr. Amey Barde for his mentorship in constructing and conducting experiments that were used to verify this model. Finally, I thank my family for their continued support in all of my endeavors, academic and otherwise.

This effort was supported by ARPA-E Award DE-AR0000140, Southern California Gas Company Grant Nos. 5660042510, 5660042538, and California Energy Commission Contract No. EPC-14-003.

Table of Contents

List of Figures

List of Tables

Nomenclature

A_c cross sectional area [m^2]

b_c baffle cut [%]

b_s baffle spacing [m]

Bi Biot number $(h_o(d_o - d_i)/k_w)$

c_p specific heat [J/kg-K]

CL tube layout constant

CTP tube count calculation

d diameter [m]

E_{th} stored energy [J]

f friction factor

h heat transfer coefficient [W/m^2-K]

H height of container [m]

j Colburn j-factor

J Bell-Delaware heat transfer correction coefficient

k thermal conductivity [W/m-K]

ℓ_w tube weld length by utilized thermal capacity $\left(\ell_w = \frac{N_t(2\pi d_o)}{Q_{cap,u}\psi_d}\right)$ $[m/MWh_t]$

L system length [m]

m mass of material [kg]

$\dot{m}$ mass flow rate [kg/s]

n specific heat ratio

N_b number of baffles

N_c effective number of tube rows crossed between baffle tips

N_{cw} effective number of tube rows crossed in the flow window

N_t number of tubes

P perimeter [m]

P_t tube pitch [m]

P_r tube pitch ratio (i.e. tube pitch normalized by tube diameter)

Pr Prandtl number

Q_{cap} storage capacity [J]

R Bell-Delaware method pressure correction coefficient, specific ideal gas constant [J/kg-K]

S_m tube bundle crossflow area [m^2]

S_w baffle window flow area [m^2]

t time [seconds]

T temperature [℃]

U energy utilization [%]

V volume [m^3]

W width of container [m]

W_f turbomachinery energy [J]

z axial location [m]

Subscripts and Superscripts

C charge

D discharge

f shell side heat transfer fluid

i inner

o outer

s sulfur

w tube wall

0 dead state value

Greek Symbols

ΔP nozzle to nozzle shellside pressure drop [Pa]

ε exergy [J]

ρ density [kg/m^3]

μ dynamic viscosity [kg/m-s]

θ tube layout (angle)

ϕ wall viscosity compensation term, $\phi = \left(\frac{\mu(T=T_w)}{\mu(T=T_f)}\right)^{0.14}$

η turbomachinery efficiency

ψ exergetic efficiency [%]

Acronyms

CSP	Concentrated Solar Power
CFD	Computational Fluid Dynamics
DOE	Department of Energy
HTF	Heat Transfer Fluid
LCOE	Levelized Cost of Energy
NPS	Nominal Pipe Size
PCM	Phase Change Material
STTB	Shell and Tube Thermal Battery
TEMA	Tubular Exchanger Manufacturers Association, Inc.
TES	Thermal Energy Storage

Chapter 1: Introduction and Background

Thermal energy storage (TES) has the potential to reduce the variability of renewable power generation and increase dispatchability. For instance, in the case of concentrating solar power (CSP), during times of intermittency such as at night or during heavy cloud cover, fuel based backup systems are commonly employed to guarantee a constant generation capacity, especially during periods of peak demand [1]. The integration of TES will allow for the removal of greenhouse gas producing fossil fuel based backup systems. Along with making CSP plants more dispatchable, TES typically has lower capital costs than mechanical and chemical methods of storage, and have been shown to substantially increase the annual capacity factor of CSP plants [2]. Outside of its use in CSP, strategies for improving the performance of combined heat and power (CHP) plants [3] have been investigated with TES in an effort to improve the overall system efficiency and cost, and future opportunities for use in waste heat recovery systems in industrial processes such as glassmaking and metallurgy exist due to the high quality waste heat produced [4]. Due to its use in a number of different industries and important role in renewable energy, there is interest in developing accurate simulation tools for the design and implementation of TES systems.

There are three main classifications of TES: sensible, latent, and thermochemical storage. Sensible TES involves storing energy in the form of temperature excursion of

storage material. Latent TES involves storing energy in the form of latent heat of fusion of storage material (typically inorganic molten salts) commonly referred to as phase change materials (PCM). An extensive review of low- and high- temperature latent TES systems can be found in the works of Lane [5], and Cardenas and Leon [4], respectively. Thermochemical energy storage takes advantage of the breaking and forming of chemical bonds during a reversible reaction in order to store and release thermal energy. While thermochemical TES is still in the research phase, it exhibits advantages such as higher energy densities than latent and sensible TES, long term storage of reactants at ambient temperatures for later recombination and energy production, and constant temperature discharge [6,7]. The current state of the art TES involves sensible storage in a two-tank system using solar salt (typically eutectic mixtures of 60% sodium nitrate and 40% potassium nitrate) [8]. While two tank systems can be used in both parabolic trough and central receiver CSP configurations up to temperatures of 565℃ without thermal degradation of the storage fluid , the relatively high capital cost of \$80/kWh_t of building these systems does not satisfy the technoeconomic target costs of less than \$15/KWh_t put forth by the US Department of Energy (DOE) and thus presents an economic dilemma [9]. The high capital cost of two-tank storage systems leads to a high levelized cost of energy (LCOE), but reductions in LCOE can be achieved by developing low cost TES using inexpensive storage materials. Latent TES with inorganic molten salt PCMs are actively being researched due to their low cost and high volumetric storage density.

However, due to the limitations in heat transfer performance during discharge, thermal performance enhancement techniques such as embedded pipes [10], heat pipes [11], metal structures [4], are incorporated, which are significant cost addition due to the greater use of metals [12].

In order for a TES system to be considered viable, it should meet the DOE goals of high heat transfer performance, a storage cost of < \$15/KWh_t, high exergetic efficiency, and low material degradation [9]. One proposed storage material for implementation in TES systems, which offers both low cost (< 15 \$/KWh_t), and high thermal and chemical stability to above 1000°C is elemental sulfur [13]. Elemental sulfur has high gravimetric and volumetric energy storage density due to contributions from sensible, latent and thermochemical enthalpies. Sulfur has a moderate vapor pressure that reduces the amount of material necessary for containment, and literature [14], as well as extensive laboratory pressure – temperature testing has shown this pressure to lie below 200 psig at 600℃. Due to the elemental stature of sulfur, it exhibits high chemical stability which makes it a favorable storage medium over a 30-year plant lifetime. Unlike molten salts, sulfur does not exhibit thermal degradation at high temperatures ($T > 565$℃) and can operate at higher temperatures for a superior Carnot efficiency. Finally, the nominal cost of sulfur is typically \$ 0.06/kg which is far less than typical molten salts and high temperature oils which cost between \$0.93/kg and \$5.00/kg [12,15]. The use of elemental sulfur in TES has been previously proposed by Clark and Dowling [13] as well as

Wentworth and Chen [16] due to its high heat of reaction ($\Delta H^{\circ}_{298K} = 414\ kJ\ mol^{-1}$) and common use in the Claus sulfur recovery systems. To the authors knowledge there has been no previous demonstration of sensible or latent thermal energy storage using elemental sulfur, however, previous on-sun demonstrations by Wong et al. [17] have shown that near equilibrium conversion of sulfuric acid to elemental sulfur between 650℃ and 850℃ can take place for thermochemical energy storage and power generation. The stored energy is then recovered via combustion of elemental sulfur into sulfur dioxide for combustion heat at a temperature in excess of 1000℃. While their results showed that newer decomposition catalysts suitable for temperatures greater than 650℃ are required, their analysis and results showed that sulfur based TES can provide for levelized costs of energy as low as $\$0.06/KWh_t$.

Numerous experimental and numerical studies using shell and tube configurations for TES systems have been led, especially for PCMs on the shellside. Lacroix [18] developed an experimentally validated numerical model that predicted the transient multiphase behavior of shellside PCM charged and discharged by a tubeside fluid, and found that performance was greatly affected by the shell radius, heat transfer fluid (HTF) mass flow rate and inlet temperature of the HTF. He and Zhang [19], and Trp [20] both performed experimental tests and theoretical analysis for similar TES configuration with PCM and paraffin waxes, respectively, on the shellside, and both found that the numerical results agreed very well with the experimental results. Fewer

studies have been conducted where the storage medium is on the tubeside of the shell and tube thermal battery (STTB) with the HTF flowing on the shellside. Ganapathi et al. [21] constructed a 5 kWh_t lab scale demonstration using supercritical naphthalene as the tubeside storage fluid and Tse, Lavine, Lakeh, and Wirz [22] have shown that such systems can be optimized for a maximum exergetic efficiency of 87% when using synthetic oil based HTF on the shellside. Along with conventional shell and tube style geometry, there is an interest in using intermodal shipping containers TES systems due to their standard sizing and use in global transport of products, which forms the subject of investigation in the present study.

Previous studies using air as HTF have been conducted using packed bed systems [23–26], however only few studies have investigated its use in TES systems in STTB. For this study, air is considered as HTF due to its inexpensive material cost in comparison to conventional molten salt HTF. An additional reason for using air based HTF is due to the development of volumetric receiver technologies for use in next generation central receiver systems in CSP plants [27]. Because open volumetric receivers exist in an open loop, gaseous HTF can readily be taken from ambient temperatures, heated, and used to fully charge a storage system if desired – a process that is not currently viable for closed loop molten salt based systems due to tubular receiver inlet temperature limitations.

Objective

The objective of this study is to develop a transient, two-dimensional numerical model to investigate the design and performance of a thermal energy storage (TES) system that uses low cost elemental sulfur stored isochorically in an intermodal shell and tube thermal battery (STTB) configuration. The objective is approached by first constructing the model and describing the governing equations, correlations for heat transfer and pressure drop, design parameters, and performance metrics used for evaluation. A verification of the model is demonstrated by comparing with preliminary experimental results as well as through comparison to an analytical solution for the classical Schumann model. Using the verified model, the influence of various design and operating parameters on the discharge performance of the system is evaluated. While similar studies have been conducted on dual medium TES systems [4,8,10–12], many of these studies have used expensive storage fluids that exceed the current technoeconomic goals of the US Department of Energy. The use of elemental sulfur as a storage fluid in a shell and tube style TES is a unique and novel concept that offers low cost — well below the US Department of Energy cost objective of 15 $/kWht [9] — for large scale energy storage solutions. Furthermore, while experiments and higher order models can provide accurate and comprehensive results, the short runtime of this numerical model allows for design parameters to be quickly iterated in order to provide thorough result useful for design. Overall, these results

demonstrate that there are preferred design points for the construction of a high temperature sulfur based TES system using intermodal containment.

Chapter 2: Model Analysis and Methodology

The TES configuration considered in the present study is shown in Figure 1. For this study, tubes with an outer diameter, d_o, and inner diameter, d_i, are packed with the storage medium (sulfur), arranged horizontally in a shell, and are supported via baffles that have a central spacing of b_s. Tubes are arranged with a triangular layout ($\theta = 30°$) and are separated by a tube pitch, P_t. The shell has a rectangular cross section of height, H, width, W, and length, L, with dimensions corresponding to that of a standard

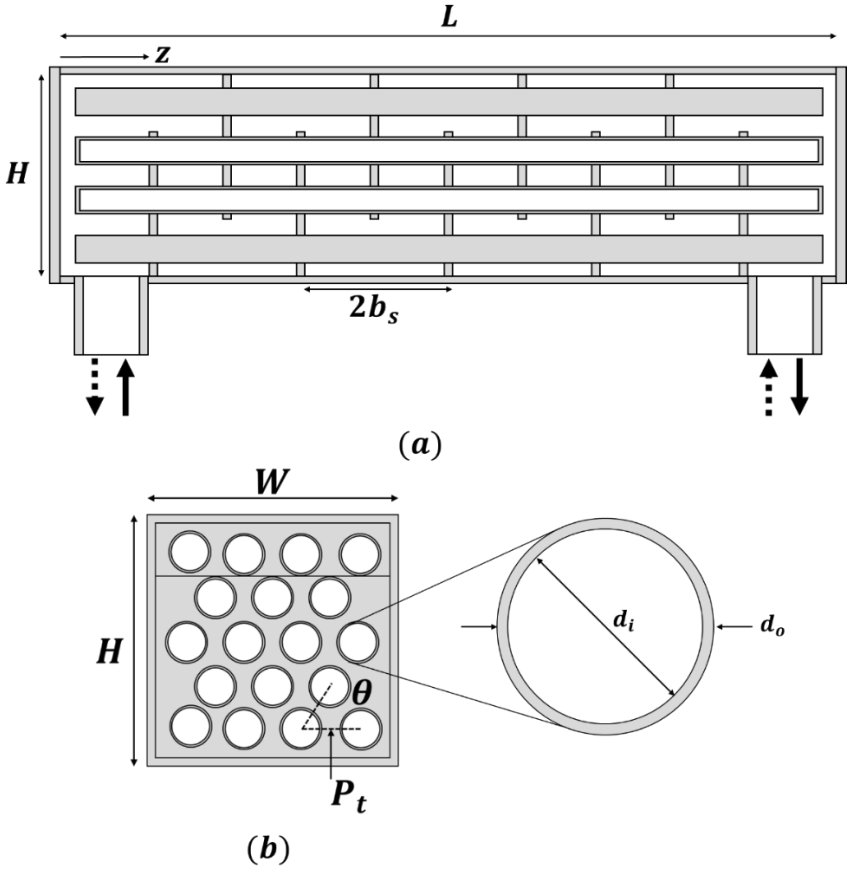

Figure 1: Schematic illustration of (a) sulfur based TES, and (b) cross sectional view of system.

intermodal shipping container [28]. The HTF flows along a tortuous path during charge and discharge with the solid (dotted) arrows indicating the direction of flow during charging (discharging). During the charging (heating) period, hot HTF enters the shell-side at the inlet located at $z = 0$, transfers heat to the cold storage fluid, and then exits at a lower temperature through the outlet at $z = L$. During stand-by period, there is no flow of HTF on the shellside and heat transfer within the system is dominated by axial conduction which acts to redistribute the axial temperature gradient formed in the system during charging. During discharge, cold HTF enters the system at $z = L$, is heated by the storage fluid, and then exits on the opposite end at $z = 0$ and, having recovered the stored thermal energy, can be used either in a power block for electricity generation or to meet industrial heating requirements.

For this analysis, the shell-side flow of heat transfer fluid is assumed to be incompressible. The outer surface of the system is assumed to be perfectly adiabatic, and the HTF temperature is assumed to be radially invariant while varying in the axial direction. The temperature of the tube wall material (stainless steel 316) and sulfur inside each tube is assumed to be spatially uniform in the radial direction while varying spatially in the axial direction at any given instant of time. The assumption of radial uniformity for any given axial location is valid for a number of reasons. For the tube wall, this is applicable due to the very low thermal resistance of thin tube walls made of a material with a high thermal conductivity leading to the Biot number being much less

Table 1: Thermo-physical properties of sulfur, wall, and HTF

Properties	Sulfur	Wall (SS 316)	Air
Density, ρ [kg/m^3]	1576.8	7798.3	0.5409
Specific heat, c [J/kg-K]	1226.5	558.3	1069.3
Viscosity, μ [kg/m-s]	-	-	$3.23e-5$
Thermal conductivity, k [W/m-K]	0.16	26.1	0.05

than 1 ($Bi \ll 1$). Additionally, for the storage medium, this is valid due to the relatively high heat transfer coefficient resulting in a relatively low thermal resistance [29]. The thermophysical properties of sulfur, steel, and air are taken to be the average value for the temperature range considered and are given in Table 1.

2.1. Numerical Model

The governing energy equations for the HTF, wall, and storage medium are denoted by Eqs. (1) - (3)

$$\left(\rho c_p A_c\right)_f \frac{\partial T_f}{\partial t} + \left(\dot{m} c_p\right)_f \frac{\partial T_f}{\partial z} = -h_o P_o \left(T_f - T_w\right) + \left(k A_c\right)_f \frac{\partial^2 T_f}{\partial z^2} \quad (1)$$

$$\left(\rho c_p A_c\right)_w \frac{\partial T_w}{\partial t} = h_o P_o \left(T_f - T_w\right) - h_i P_i (T_w - T_s) + \left(k A_c\right)_w \frac{\partial^2 T_w}{\partial z^2} \quad (2)$$

$$\left(\rho c_p A_c\right)_s \frac{\partial T_s}{\partial t} = h_i P_i (T_w - T_s) + \left(k A_c\right)_s \frac{\partial^2 T_s}{\partial z^2} \quad (3)$$

where $\dot{m}_f$, ρ, c_p, k, and T refer to the mass flow rate, density, heat capacity, thermal conductivity, and temperature, respectively, of the HTF, tube wall, or sulfur storage fluid. Geometric terms such as A_c and P refer to the axial cross section and perimeter, respectively, where P_o refers to the outer perimeter of tubes which are in contact with the HTF and P_i refers to the inner perimeter of tubes which are in contact with the storage fluid. For this study, the tube outer diameter and wall thickness are chosen based on the nominal pipe size (NPS) standard whose values are based on ASME standards B36.10M and B36.19M [30]. The interstitial heat transfer coefficients between the HTF and tube walls and the tube walls and storage fluid are represented by h_o and h_i, respectively. For Eqs. (1) - (3), f refers to the heat transfer fluid, w refers to the wall, and s refers to the storage material (sulfur).

The interstitial heat transfer coefficients are obtained from two different sources. The tubeside heat transfer coefficient is a function of the tubeside Rayleigh number and is obtained via an experimentally validated CFD model, the details of which can be found in the works of Nithyanandam et al. [29]. The shell-side heat transfer coefficient can be represented using a number of different methods. For systems utilizing shell and tube style heat exchangers – which have analogous shellside geometry to that of STTB – several studies have employed Kern's method [31], the Bell-Delaware method [32], and Wills-Johnson method [33] in order to quantify the shell-side heat transfer coefficient and pressure drop. For this study, the Bell-Delaware method is utilized because it takes into

account the effect of various geometric terms such as baffle cut, b_c, baffle spacing, b_s, number of baffles, N_b, tube pitch, P_t, and tube diameter, d_o. Furthermore, the Bell-Delaware method presents a methodology to calculate coefficients that accounts for factors such as baffle window flow effects, interfacial leakages, bundle bypass, unequal baffle spacing, and laminar or transitional flow which in this study will be encompassed by the coefficients J and R. The corrected heat transfer coefficient is denoted as:

$$h_o = J\phi c_{p,f} j \frac{\dot{m}_f}{S_m} \mathrm{Pr_f}^{-2/3} \quad (4)$$

where S_m is the crossflow area at the shell centerline and is represented by $S_m = b_s\left[\frac{(W-d_o)}{P_t/d_o}(P_t/d_o - 1)\right]$, $\mathrm{Pr_f}$ is the Prandtl number for the shell-side fluid, ϕ is the wall viscosity compensation term ($\phi = \left(\frac{\mu(T=T_w)}{\mu(T=T_f)}\right)^{0.14}$) and j is the Colburn factor which is based on empirical measurements of tube banks in crossflow [34,35]. The nozzle to nozzle pressure drop, ΔP, which encompasses the pressure drop due to crossflow, axial flow within the window, and cross flow at the inlet and outlet of the system, can be represented by:

$$\Delta P = \left[(N_b - 1) + R\left(1 + \frac{N_{cw}}{N_c}\right)\right]\left(\frac{2fN_c}{\rho\phi}\left(\frac{\dot{m}_f}{S_m}\right)^2\right) + \left(\frac{(2+0.6N_{cw})\dot{m}_f^2}{2\rho S_m S_w}\right) \quad (5)$$

where N_c, and N_{cw} is the effective number of tube rows crossed between baffle tips and in the flow window, respectively, f is the friction factor, and S_w is the net crossflow area through one baffle window given by $S_w = WH - \frac{N_t \pi d_o^2}{4} b_c$. For a shell and tube style heat exchanger, the effective number of tube rows crossed between baffle tips and in the flow

window are a function of the shell geometry, and can be determined as $N_c = H(1 - 2b_c)/P_t$ and $N_{cw} = 0.8b_cH/P_t$ based on calculations by Bell et al. [34]. The Bell-Delaware correlation is valid for heat exchangers with square pitch, rotated square pitch, and triangular pitch layouts, and for $1 \leq Re_D \leq 10^5$. The friction factor, f, and Colburn factor, j, are correlated by Taborek [35] and its coefficients are dependent on the tube layout, tube pitch ratio ($P_r = P_t/d_o$), Reynolds number.

$$j = a_1 \left(\frac{1.33}{P_r}\right)^a Re_D^{a_2} \quad (6)$$

$$f = b_1 \left(\frac{1.33}{P_r}\right)^b Re_D^{b_2} \quad (7)$$

The coefficients of Eq. (6) and (7), are tabulated based on empirical results from testing with shell and tube heat exchangers and further details can be found in the works of Bell [32]. For calculation of heat transfer between the HTF and tubes, the thermophysical properties of the HTF are shown to greatly affect the shellside heat transfer coefficient and pressure drop. Thus for calculation of the shellside pressure drop and heat transfer coefficient variable properties are considered and their temperature dependencies are captured via 4th order polynomial curve fits. For air HTF this data is given by Bergman et al. [36], and the equations are given in Table 2.

The pressure drop across the STTB directly affects the turbomachinery energy, W_f, required to move the HTF (air) through the system during charging and discharging which in turn affects the overall efficiency of the TES system. Because air can be expressed

Table 2: Variable properties for shellside HTF coefficient and pressure drop calculations

Properties	Air HTF
Density, ρ [kg/m^3]	$(1.52e-12)T^4-(7.35e-9)T^3+(1.29e-5)T^2-9.91T+3.243$
Specific heat, c [J/kg-K]	$(1.12e-13)T^4-(5.35e-10)T^3+(8.27e-7)T^2-(2.95e-4)T+1.0321$
Viscosity, μ [kg/m-s]	$(-3.97e-13)T^4+(2.15-9)T^3-(4.70e-6)T^2+(6.99e-3)T+0.109$
Thermal conductivity, k [W/m-K]	$(3.23e-13)T^4+(1.96e-9)T^3-(5.16e-6)T^2+(1.03e-2)T-0.0640$

as a compressible ideal gas, it can be treated as an isentropic process [38]. This work can be expressed as:

$$W_f = \int_{t_0}^{t_c} \dot{m}_{f,c} \frac{w_c}{\eta} dt + \int_{t_c}^{t_d} \dot{m}_{f,d} \frac{w_d}{\eta} dt \quad (8)$$

where t_o is the initial time and the overall turbomachinery efficiency, η, is taken to be the product of the isentropic compressor efficiency, η_c, and the energy conversion efficiency, η_{ec}, (i.e. $\eta = \eta_c \times \eta_{ec}$). The specific work terms, w, during the charge and discharge cycle are represented as:

$$w_c = -\frac{nRT(z=L)}{n-1}\left[\left(\frac{P(z=L)}{P(z=L)+\Delta P}\right)^{\frac{n-1}{n}} - 1\right] \quad (9)$$

$$w_d = -\frac{nRT(z=0)}{n-1}\left[\left(\frac{P(z=0)}{P(z=0)+\Delta P}\right)^{\frac{n-1}{n}} - 1\right] \quad (10)$$

where n is the HTF heat capacity ratio ($n = c_p/c_v = 1.4$) and R is the specific ideal gas constant of air ($R = \bar{R}/M_{air} = 287.058$).

The boundary conditions of the model during charging and discharging are specified as:

$$T_f(z=0) = T_c,\ \frac{\partial T_f}{\partial z}(z=L) = 0; Charging \quad (11)$$

$$\frac{\partial T_f}{\partial z}(z=0) = 0,\ \frac{\partial T_f}{\partial z}(z=L) = 0; Standby \quad (12)$$

$$T_f(z=L) = T_d,\ \frac{\partial T_f}{\partial z}(z=0) = 0; Discharging \quad (13)$$

Different operating scenarios are considered for this study, however for the first charge (discharge) process the tank is assumed to start from a completely discharged (charged) state. For this study the charge temperature, T_c, using air HTF is taken to be 600℃ and the discharge temperature is taken to be 200℃, which is well within the temperature range that open volumetric receivers can maintain and is within the material limitations of the tube material, stainless steel 316 [27].

Eqs. (1) - (3) are discretized using a finite volume approach. A hybrid scheme is used to discretize the convective terms, while the diffusion terms are discretized using a central differencing scheme under the assumption of a piecewise-linear profile. Time-stepping of the unsteady term is via a first order fully implicit scheme [39]. A systematic grid and time step study resulted in using 1000 axial nodes and a non-dimensionalized time step, $\Delta t^* = \frac{\Delta t}{\Delta z}\frac{\dot{m}}{\rho S_m}$, of 4.049×10^4 for a discretization error of 0.004% and 0.59%,

respectively, and further details of this study are provided in the numerical model verification section in Chapter 2.

2.2. Model Inputs and Outputs

The numerical model described is used to study the various heat transfer processes that occur within the system which affect the overall performance of the thermal energy storage system. These heat transfer processes include the shell-side convective heat transfer between the shell and tube bank, the convective heat transfer between the tube walls and storage fluid, as well as the axial conduction within the HTF, wall, and storage fluid. From these calculations, the transient axial temperature field for the HTF, wall, and storage fluid can be determined as well as auxiliary outputs such as the shell-side pressure drop and heat transfer coefficient. The contributions from sensible, latent and thermochemical enthalpies of sulfur in the temperature range of interest are captured by the effective heat capacity, c_p, of sulfur, and simulations in which sulfur is a single phase liquid system are shown to agree very well with experimental results [29]. Further energy storage within the system is due to storage within the tube walls and heat transfer fluid, which are both shown to be non-negligible. The amount of energy stored within the system (E_{th}) at any time step is represented as:

$$E_{th}(t,T) = \sum_{i=1}^{n} \left(m_s c_{p_s} \left(T_{s(i)} - T_D \right) + m_w c_{p_w} \left(T_{w(i)} - T_D \right) + m_f c_{p_f} \left(T_{f(i)} - T_D \right) \right) \Delta z \qquad (14)$$

where m is the mass of the material, i represents the axial node, and n corresponds to the total number of discretized axial volumes. The amount of energy stored for any given time step is referenced with respect to the discharge temperature, T_D, of the system, and in the fully discharged state there is a net storage of zero.

A number of different metrics have been used to evaluate the charge, storage, and discharge performance of a thermal energy storage system including the utilization and exergetic efficiency. The utilization of a system is a measure of how well the system can store and recover heat within a system, and numerous authors have given different definitions for the discharge, charge, and full cycle utilization of which Jegadheeswaran provides a concise review [40]. For this study, a single discharge from a fully charged state is evaluated in order to determine the maximum possible utilization, and thus the discharge utilization, U, is defined using the definition of energy efficiency by Rosen [41]. The discharge utilization is defined as the ratio of the energy recovered from the system and the initial energy within the system:

$$U = \frac{\int_{t_o}^{t_d} \dot{m}_{f,d} c_{p_f} \left(T_{f,in} - T_{f,out}\right) dt}{E_{th}(t = t_o)} \quad (15)$$

From the utilization, the utilized storage capacity, $Q_{cap,U} = U \times Q_{cap}$, of a system can be found in comparison to its rated capacity, and can be useful in comparing between systems that may vary in capacity. While the utilization can provide a measure of energy stored, it is inadequate in providing information on the quality of the energy and how useful it is in relation to the surrounding conditions. Exergetic efficiency is a metric that

has been used in several studies to quantify the amount of useful energy provided by a system [22,40,42–44]. In general, the amount of exergy within the system at any given timestep can be represented as:

$$\varepsilon(t,T) = \sum_{i=1}^{n} \left(m_s c_{p_s} \left[\left(T_{s(i)} - T_D \right) - T_0 \, ln \left(\frac{T_{s(i)}}{T_D} \right) \right] + m_w c_{p_w} \left[\left(T_{w(i)} - T_D \right) - T_0 ln \left(\frac{T_{w(i)}}{T_D} \right) \right] + m_f c_{p_f} \left[\left(T_{f(i)} - T_D \right) - T_0 \, ln \left(\frac{T_{f(i)}}{T_D} \right) \right] \right) \Delta z \quad (16)$$

where T_0 is the dead state temperature and for this study is taken to be 27℃. Similar to the utilization, the discharge exergetic efficiency, ψ_d, is given by Rosen and defined as the total amount of exergy recovered, ε_r, from the system minus exergy destroyed, ε_d, normalized by the initial exergy within the system at the start of the discharge period [42]. This can be defined mathematically as:

$$\psi_d = \frac{\int_{t_o}^{t_d} \dot{m}_{f,d} c_{p_f} \left(T_{f,out} - T_D - T_0 \ln \left(\frac{T_{f,out}}{T_D} \right) \right) dt - \int_{t_o}^{t_d} \dot{m}_{f,d} \frac{w_d}{\eta} dt}{\varepsilon(t_d, T)} \quad (17)$$

The overall performance of the system is directly affected by various geometric terms such as baffle spacing, tube pitch, tube diameter, etc. as well as operational conditions such as mass flow rate. The following sections will provide an evaluation of the system performance based on these metrics.

Chapter 3: Results and Discussion

3.1. Numerical Model Verification

The numerical model is verified in a number of manners. Firstly, a timestep and grid size dependency study are conducted in order to reduce the discretization error of the model. Following this study, the physics of the model is verified by two methods. The first method involves comparing the model with experimental results from a single tube sulfur storage system. The results of this experiment were used to verify the physics relating to the tubeside heat transfer. The second method involves comparison with the analytical solution of a dual-medium storage system based on a single phase conductivity model. Model verification was done in this manner because, to the authors knowledge, no experimental results for dual-medium storage system using a static storage fluid on the tubeside of a STTB have been adequately reported in the literature which would provide a direct method of validation. In order to mediate this, the Energy Innovation Laboratory is currently constructing a 10 kWh_t lab scale demonstration that has a scaled down analogous geometry to the system shown in Figure 1, and the experimental results of this setup will be used to provide future validation to this numerical model.

Prior to verification a grid size dependency study and timestep study were completed to reduce the discretization error. For this study, the number of axial nodes was increased until the discretization error was relatively small, and further grid

refinement led to increased computational cost without providing much more accurate results. The timestep study was undertaken in the same manner, in which the dimensionless timestep, $\Delta t^* = \frac{\Delta t}{\Delta z}\frac{\dot{m}_f}{\rho S_m}$, was decreased until further refinement did not yield relatively more accurate results. A non-dimensionalized timestep is used here to account for the effect that the shellside geometry and HTF has on the crossflow velocity and residence time of the fluid which would not be captured via calculation of Δt. Figure 2a and Figure 2b show the results of said studies for a system with $d_o = 0.06\,m$, $b_S = 0.5\,m$, $P_r = 1.5$, $\dot{m}_f = 0.5\,kg/s$, with all other geometric properties given by Table 3. The result of this study is a system with 1000 axial nodes and a nondimensionalized time step, $\Delta t^* = \frac{\Delta t}{\Delta z}\frac{\dot{m}}{\rho S_m}$, of 4.049×10^4 for a discretization error of 0.004% and 0.59%, respectively.

A schematic image of the experimental setup used as the first method of model

Table 3: Design and operating parameters for single discharge study

Parameter	Symbol	Range/Value
Tube Pitch Ratio	P_r	$1.2 - 1.5$
Baffle Spacing	b_s	2" (0.05 m) - 20" (0.51 m)
Tube Outer Diameter	D_o	2" NPS (0.06 m) - 8" NPS (0.22 m)
Mass Flow Rate	$\dot{m}_f$	$0.4\,kg/s - 3\,kg/s$ (air)
Baffle Cut	b_c	15%
Tube Layout Angle	θ	30°
System Width	W	$2.385\,m$
System Height	H	$2.352\,m$
System Length	L	$5.867\,m$

is shown in Figure 3. A one meter long, two inch nominal pipe size ($d_o = 0.06\ m$) schedule 40, stainless steel 316 tube was filled with 3.14 kg of sulfur. Two stainless steel 316 caps are machined to provide access ports for instrumentation tubes with three on either end. These instrumentation tubes are used to provide access to 6 K-type thermocouples with three inserted 11.3″ from the left side of the system and three inserted from the right side of the system with two of those inserted 11.3″ inside and one inserted 8″ inside. The system is heated at the tube wall using eight 300 W heater tapes controlled using PID controllers and covered with ceramic fiber insulation in order to minimize thermal losses to the environment. The surface temperature of the tube was measured using sixteen k-type thermocouples evenly spaced out two inches apart from one another along the entire length of the tube. An experiment was conducted in which the entire tube was heated to 200℃ and a thermal gradient was applied to the tube. The

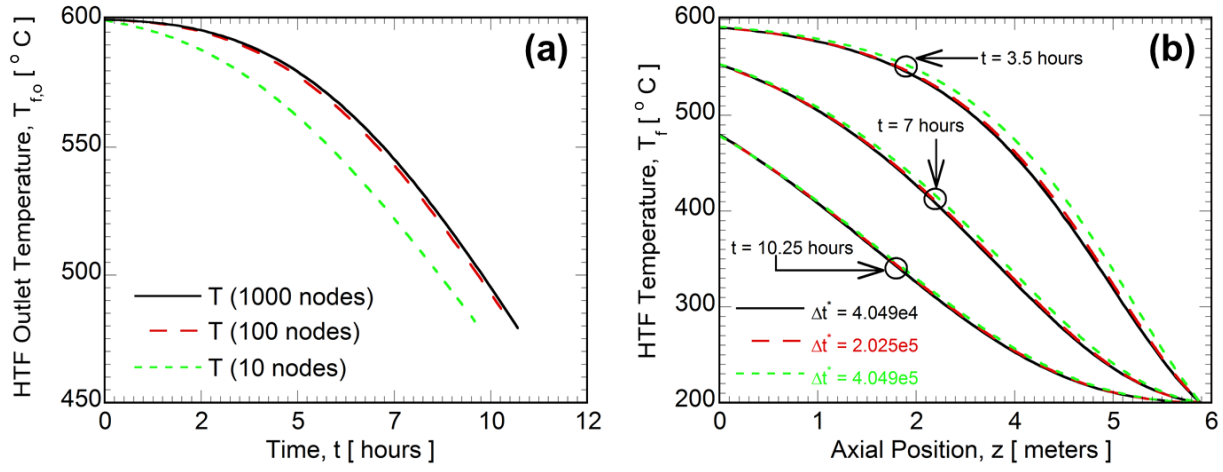

Figure 2: Dependency of numerical solution on (a) grid size, Δz, and (b) non-dimensional timestep, Δt^*.

thermal gradient was created by varying the setpoint temperature of each heater tape in 50°C increments between the range of 250°C to 600°C. Once a thermal gradient was created along the tube, a progressing axial temperature gradient was simulated. Over time, as the system charged, the setpoint would be increased in 50°C increments until every heater tape had reached a maximum temperature of 600 °C. This was done to approximate the motion of a thermocline that is typically seen in the storage material and heat transfer fluid in a dual-medium TES system. Due to the experimental setup not involving a HTF, in order to account for heat transfer between the HTF and wall in the numerical model, the interstitial shell side heat transfer coefficient, h_o, was set to an arbitrarily high heat transfer coefficient of 10^{14}, and the shellside mass flow rate was set to zero. By doing this, the surface temperature recorded by the experiment could be used as the wall boundary condition inside the model. Validation using this test is shown in Figure 4, with the markers indicating the experimental results and the lines corresponding to results obtained via the model. The model shows good agreement, with the maximum relative

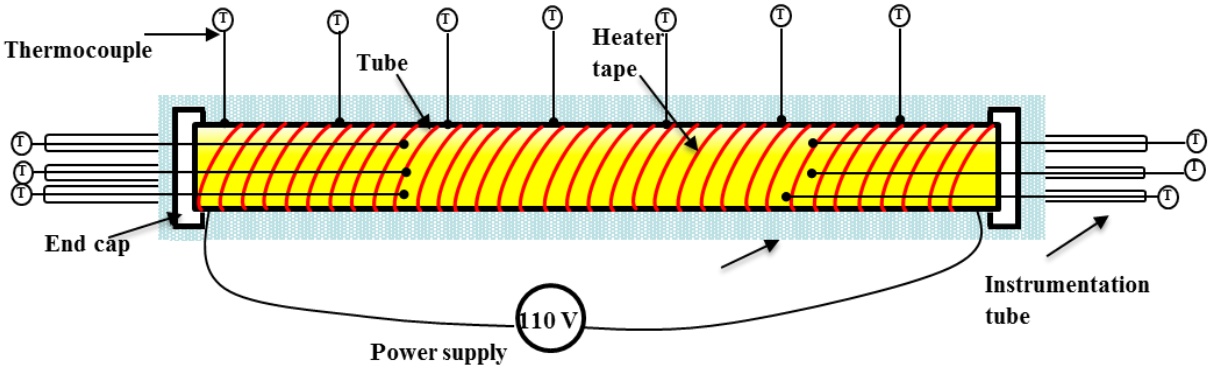

Figure 3: Schematic image of experimental system used for verification.

error between the numerical results and the experimental results in Figure 4a being 2.3% and the average error obtained from the Euclidean norm being 2.14%.

For further verification, the numerical model was compared with the analytical solution of a simplified Schumann model governing flow of air in a dual-medium storage unit as given by Riaz [45]. The simplified Schumann model makes a number of different assumptions in order to arrive at an analytical solution. Firstly, axial thermal diffusion of the HTF is assumed to be negligible because of the low thermal diffusivity of the air HTF. Secondly, the volumetric heat transfer coefficient is assumed to tend to infinity corresponding to good heat transfer between the air HTF and storage medium. As the volumetric heat transfer coefficient tends to infinity, the air HTF temperature and storage medium temperature coalesce to the same temperature, and the energy equations governing to air HTF and packed bed reduce to a single equation. The energy equation becomes an unsteady convection-diffusion equation with convection affected by the one-dimensional axial flow of air HTF and diffusion affected by axial thermal diffusion through the storage medium. For this solution, the material properties of the wall were taken to be that of the storage fluid, and the volumetric interstitial heat transfer coefficient between the air and storage material was set to an arbitrarily high heat transfer coefficient of $10^{14}\ W/m^2K$. Further adjustments of the numerical model such as neglecting the HTF conduction term were made in order to reduce it to a system that was equivalent to the simplified Schumann model solved by Riaz [45]. A Danckwert type inlet boundary

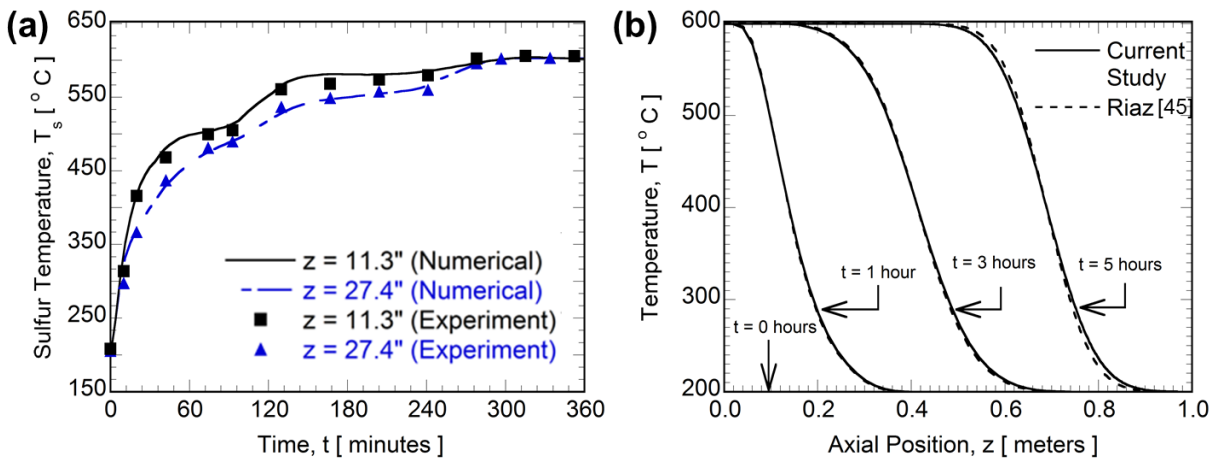

Figure 4: Comparison of numerical results with experimental and analytical methods Comparison was done using experimental results from (a) progressing thermal wave boundary condition. Comparison with analytical results for a single phase conductivity model by Riaz [45] is shown in (b).

condition, namely $\frac{\partial T_f}{\partial z}(z=0) = \frac{\dot{m}_f c_{p_f}}{A_{c_f} k_s}(T_f - T_C)$, was used in the numerical model to allow for comparison with the analytical solution. For comparison, a test case involving a 1-meter-long system, with $W = 2.352\,m$, $H = 2.385\,m$, $P_r = 1.2$, and $d_o = 0.06\,m$ was considered. Comparison between the numerical model and the corresponding results using the analytical solution are shown in Figure 4b, and the relative error between their results is at a maximum 1.01% and the average error obtained from the Euclidean norm is 0.13%.

3.2. Single Charge, Standby, Discharge Cycle

Prior to conducting a parametric study of a single discharge situation, the response of the system to a single six hour charge, twelve hour standby, and six hour discharge operation is investigated using a parametric combination of $P_r = 1.2$, $d_o = 0.06\ m$, $\dot{m}_f = 1.7\ kg/s$, and $b_S = 0.5\ m$ in order to demonstrate the flexibility of the model and explain typical trends seen.

Figure 5a displays the axial temperature variation of the HTF (solid line) and storage material (dashed line) for different times during charging. At the start of charging, the STTB is initially in a fully discharged state ($T = 200$°C) and there is no flow of fluid through the system. At $t = 0$, HTF enters the system at $z = 0$ and energy is transferred between the HTF and solid material (steel tubes and sulfur). As the HTF gives up its energy, the heat transfer downstream becomes less effective resulting in a nonlinear axial temperature profile. Initially this temperature profile is characterized by HTF near the inlet being at the charge temperature ($T_f(z = 0) = T_C$), HTF at the outlet being near the discharge temperature ($T_f(z = L) = T_D$), and the temperature field of the intermediary forming as a result of the stratification of the hot and cold fluid, as typically seen in thermocline storage systems [46]. As charging progresses, the pre-existing cold fluid is discharged from the system and the stratification layer moves across the system. At some point during charging, the outlet temperature will no longer be at the discharge temperature and will begin to increase as the stratification layer reaches the outlet. This temperature profile is also seen in the sulfur, however this profile lags behind the air

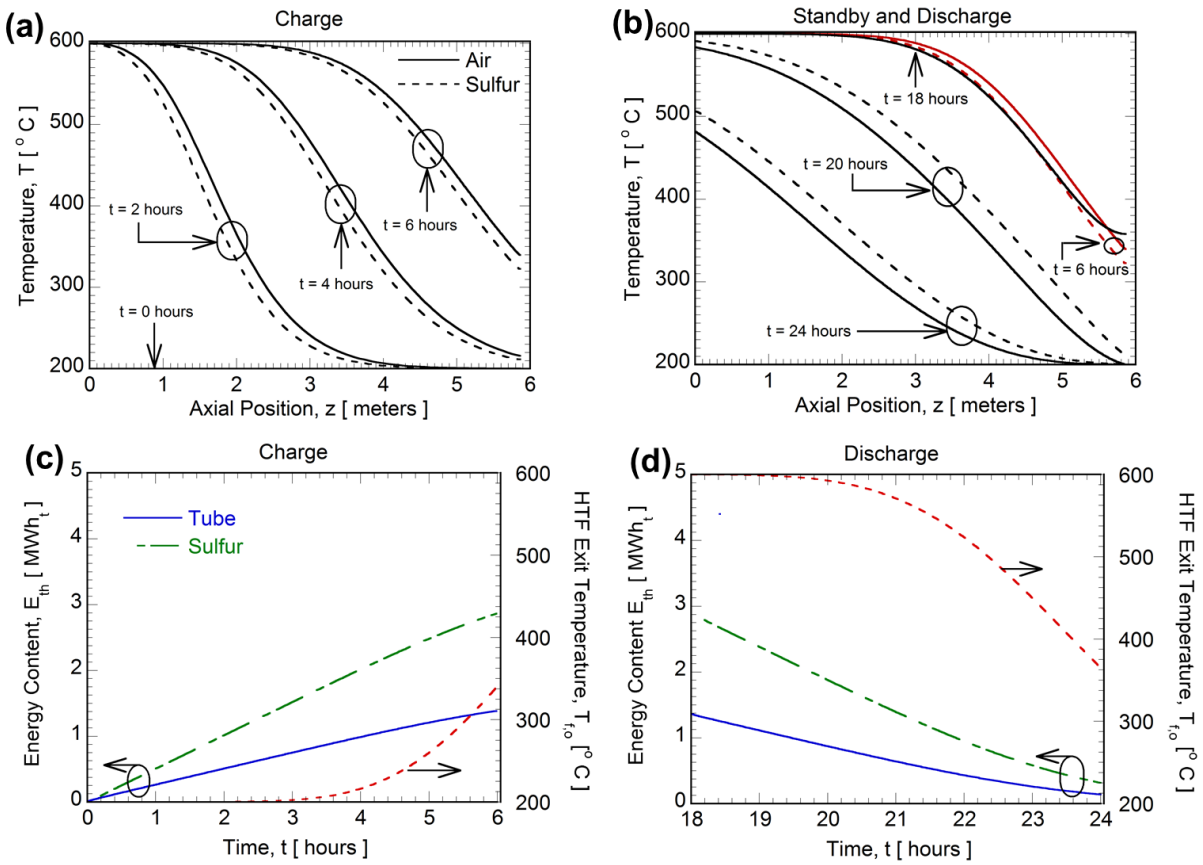

Figure 5: Axial temperature variation of HTF (solid) and sulfur (dashed) during (a) charging and (b) standby and discharging. The temperature profile at the end of charging/beginning of standby ($t = 6\ hours$) is shown in red in (b). Energy stored in tube wall and sulfur as well as HTF outlet temperature during (c) charging and (d) discharge.

temperature profile due to sensible heat storage in the tube wall material, as well as due to thermal resistance between the HTF and sulfur. The twelve-hour standby period is shown in Figure 5b. At the end of charging (t = 6 hours), the flow of HTF is halted and the system dynamics are dictated by axial conduction. Due to the assumption of a well-insulated system, there are no thermal losses to the environment, and all temperature changes within the system are due to heat transfer between the sulfur, tube material, and

HTF. At the end of the standby period (t = 18 hours) there is a slight flattening of the axial temperature profile due to redistribution of energy within the system, which affects the initial temperature field and overall performance during discharge. Figure 5b also displays the axial temperature variation of the HTF and storage material for various times during discharge. At t = 18 hours, HTF enters the system at $z = L$, energy stored inside the storage material (tube wall and sulfur) is recovered by the HTF, and the heated HTF exits the system at $z = 0$. Just as in charging, there is a nonlinear temperature profile that forms in the HTF and the storage material due to the HTF progressively recovering energy from the system, and a delay in the storage material is observable due to the initial recovery of sensible energy in the tube wall material. Ultimately, this discharge process continues until $t = 24\ hours$ at which point the simulation is ended.

Energy storage within the tube and storage material and the temporal variation in the HTF outlet temperature is shown in Figure 5c – d. During charging (Figure 5c) there is a near linear increase in the overall energy stored in the system over time despite there being a nonlinear temperature profile within the system. This is due to the overall energy being placed into the system (Eq. 14) being constant until the HTF outlet temperature ($T_f(z = L)$) begins to increase at approximately 4 hours. The standby period (Figure 5d) is characterized by the energy stored within the system being constant due to the assumption of an adiabatic wall condition. Additionally, due to the near similar temperature distribution within the HTF, tube material, and storage fluid, there is little

redistribution of thermal energy between the three media. In the interest of conciseness, the standby period energy vs time plot is not shown here. The discharge period is displayed in Figure 5d. The declining heat transfer temperature ($T_f(z=0)$) after $t = 19$ hour leads to a non-linear decay in energy storage due to the overall decrease in utilization (Eq. 15). Under ideal conditions, all of the thermal energy inside the system should be recovered during the discharge process, however, due to the thermal resistance within the HTF, tube wall, and storage material there is still some thermal energy within the system at the end of discharge.

The results of the single charge, standby, and discharge cycle show that charging is more efficient than discharging due to the steeper thermocline allowing for higher utilization of energy. Additionally, the standby period is of negligible importance due to the adiabatic wall boundary condition leading to energy being conserved within the system. For these reasons, the overall discharge efficiency will be discussed further with a single discharge parametric study.

3.3. Parametric study for single discharge

With the numerical model verified, a thermal storage system is designed with the goal of finding the most optimum setup for extending the utilization of a power plant, which in this case is a solar power tower equipped with an open volumetric receiver coupled to a Rankine steam power cycle. The storage system itself is agnostic to the heat

input and demand, and a solar power tower and Rankine steam power cycle are considered in order to minimize the number of design and operating parameters for study. The range of design and operating parameters chosen for the TES system are based on typical design ranges seen in shell and tube heat exchangers [34] as well as from typical design constraints chosen for TES in CSP plants [9]. Due to the desire to use standard sizes in order to reduce manufacturing costs and easily transport TES systems the shell height, width, and length are chosen here to correspond to the dimensions of a 20′ standard intermodal container [28].

A parametric study for a single discharge situation is discussed here in which the system starts at a fully charged state ($T = 600℃$) and is discharged by flowing air through the system at the discharge temperature ($T_D = 200℃$). Because thermocline TES systems exhibit a temperature decline during the discharge process which leads to a decrease in the exergetic efficiency and utilization, two different cutoff criteria are considered. The first cutoff criterion is chosen to be when the HTF outlet temperature falls below the cutoff temperature ($T_c = 480℃$). The temperature cutoff value is chosen based on the requirement that the moisture content of steam at the exhaust of a steam turbine must not exceed 10%, and an analysis using a simple ideal Rankine steam cycle demonstrates that 480℃ is an agreeable cutoff temperature for a system of this storage capacity [25]. The second cutoff criterion is chosen to occur when the exergy destruction rate due to heat transfer and turbomachinery work exceeds that of the exergy recovery rate from the

system during discharge (i.e. the integrand in the numerator of Eq. 17 is zero). To demonstrate the second criterion, the temporal variation in exergy recovered, exergy destroyed, and HTF outlet temperature for the case of $\dot{m}_f = 1.00\ kg/s$, $d_o = 0.06\ m$, $P_r = 1.2$, and $b_s = 0.14\ m$ is shown in Figure 6. Initially, due to the use of variable properties in calculating the pressure drop of the shellside HTF, the rate of exergy destroyed, ε_d, will decay with temperature during discharge. As the thermocline layer begins to reach the outlet of the system, the exergy recovered, ε_r, will also begin to decay. As the outlet temperature increases, the compressor work calculated via Eq. (8) will increase slightly due to the outlet pressures dependence on the outlet temperature, causing additional exergy destruction. For the case considered, the exergy destroyed begins to exceed the exergy recovered before the first criterion is met and it is not sensible to continue heat recovery past this point.

Figure 7 displays the axial temperature profiles of the storage fluid at the end of discharge for the range of parameters shown in Table 3 and with default parameters given as $P_r = 1.2$, $d_o = 0.06\ m$, $\dot{m}_f = 1.75\ kg/s$, and $b_S = 0.50\ m$. The variation in the final axial temperature profile in the storage material for variable $\dot{m}_f$ is shown in Figure 7a. For the range of mass flow rates considered the discharge utilization lies between 85.42% and 77.52% for the range of $\dot{m}_f = 0.40\ kg/s$ to $\dot{m}_f = 3.0\ kg/s$, respectively. The trend of increased utilization with decreased HTF mass flow rate is due to the increased residence time of fluid within the system which ultimately allows for increased interaction of the

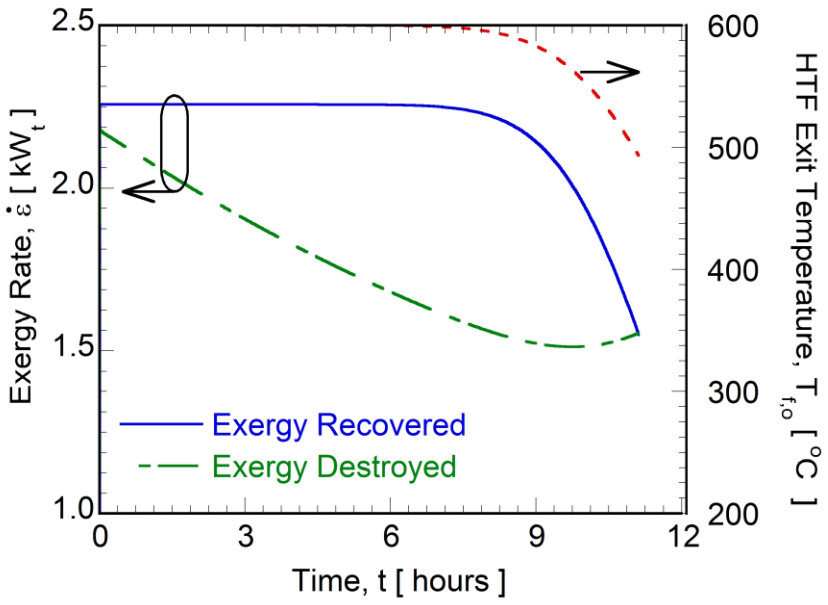

Figure 6: Exergy destruction and recovery, and HTF outlet temperature vs time for $\dot{m}_f = 1\ kg/s$, $d_o = 0.06\ m$, $P_r = 1.2$, and $b_s = 0.14\ m$. For this situation, discharge is discontinued at the point at which exergy destruction is equivalent to exergy recovered.

HTF with the storage material for energy recovery during discharge. Furthermore, for a dual-medium storage system, a low mass flow rate results in a relatively low Reynolds number and steeper thermocline [47] which allows for higher quality heat to be recovered and for the temperature cutoff condition to be delayed for higher system utilization.

The effect of tube diameter on the final axial temperature profile is shown in Figure 7b. While increasing tube diameter is shown to result in an increased tubeside Nusselt number – suggesting efficient convective heat transfer between the tube wall and storage material – the resulting heat transfer coefficient is lower due to the heat transfer coefficients inverse relationship with tube diameter. Additionally, larger tube diameters result in a decreased volume of tubes within the heat exchanger and thus a decrease in

surface area in which convective heat transfer can take place. This ultimately increases the overall thermal resistance of the system and results in a lower discharge utilization. Thus more energy is utilized within the system with $d_o = 0.06\,m$ ($U = 84.25\%$) vs $d_o = 0.22\,m$ ($U = 60.05\%$).

The effect of baffle spacing on the discharge axial temperature profile is shown in Figure 7c. Baffle spacing, b_s, is shown to have little effect on the final temperature gradient and utilization within the system. However, because pressure drop scales

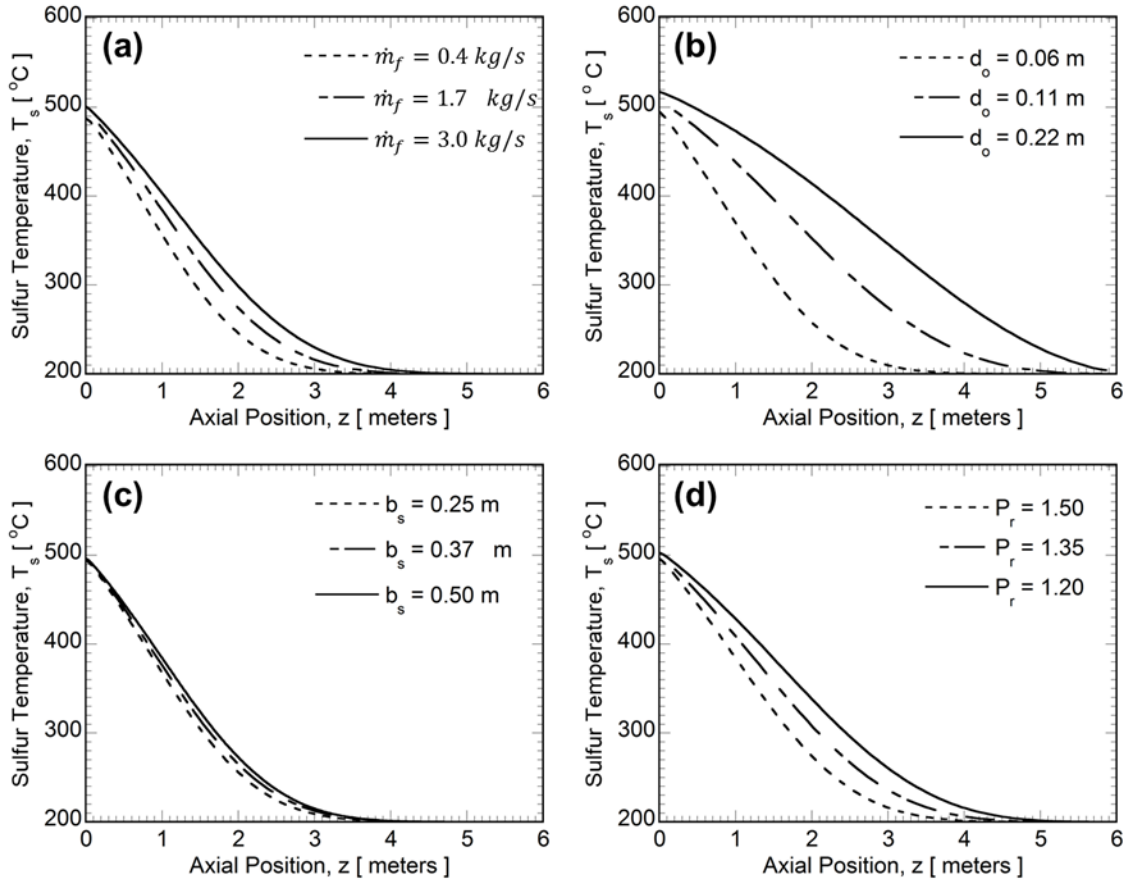

Figure 7: Axial temperature gradient within storage material (sulfur) at the end of discharge for variable (a) mass flow rate, (b) tube outer diameter, (c) baffle spacing, and (d) tube pitch ratio.

nonlinearly with baffle spacing, low baffle spacing can result in a high pressure drop and lead to a high amount of exergy destruction due to compressor work. Based on the trade-offs between increase in compressor work and heat transfer performance, the optimal baffle spacing should be determined, and will be discussed later.

The final subplot, Figure 7d, shows the effect of tube pitch ratio, $P_r = P_t/d_o$, on axial temperature gradient. Increased tube pitch has two major effects on the system. First, for a fixed shell size, the overall storage capacity within the system decreases with increasing tube pitch ratios due to less tubes fitting within the system. According to Kakaç and Liu [48], the number of tubes within a system can be determined as $N_t = \frac{WH}{(P_r d_o)^2}\frac{CTP}{CL}$ which is based on the projected area of tubes within a shell cross section. The variable CTP corresponds to the number of tube passes within the system while CL corresponds to the tube layout, and for this study they are taken to be 0.93 and 0.87, respectively, in order to correspond to a system with a single tube pass and layout of 30° [34]. The rated capacity of a system is highly dependent on P_r, and a system with $d_o = 0.06\,m$ and $P_r = 1.5$ is rated for 3.21 MWh_t whereas a system with $d_o = 0.06\,m$ and $P_r = 1.2$ is rated for 5.03 MWh_t. In addition to an increased capacity with decreased tube pitch ratio, as the tube pitch ratio is decreased, the clearance between tubes, c = $P_t - d_o$, also decreases. This increases the crossflow Reynolds number and the overall heat transfer coefficient in accordance to Eq (4) and (7) allowing for superior convective heat transfer. However, despite an increase in the heat transfer coefficient, an increased Reynolds

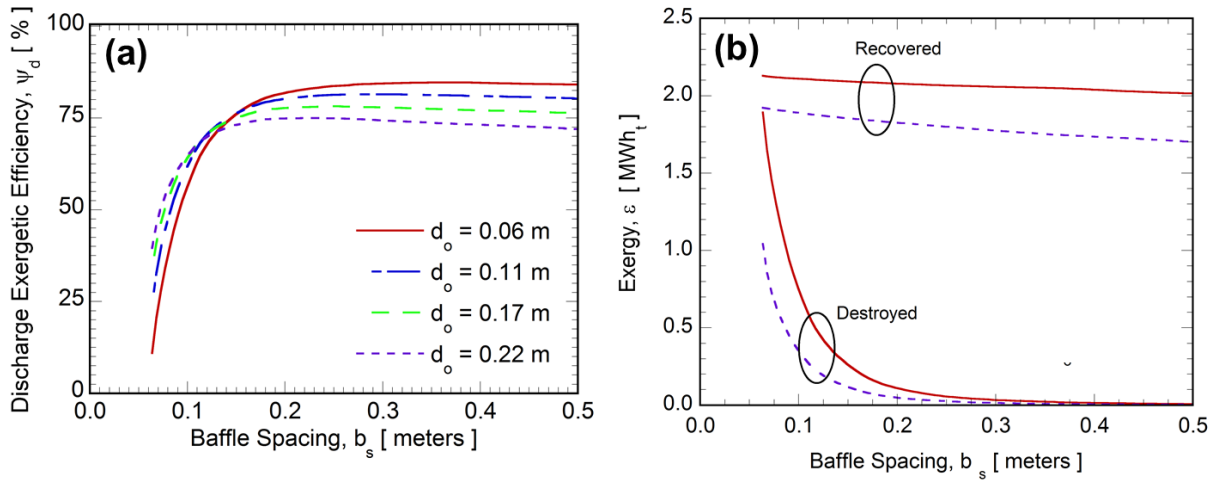

Figure 8: (a) Exergetic efficiency and (b) exergy recovered and destroyed within the system vs baffle spacing for the case of $\dot{m} = 0.4\ kg/s$. Exergy destruction decreases exponentially with baffle spacing due to its reliance on pressure drop.

number leads to a decreased residence time of HTF within the system and leads to a lower utilization of energy.

Since Figure 7c shows that the baffle spacing does not greatly affect the utilization, and in order to limit the number of parameters for study, an initial study of baffle spacing was conducted prior to a full parametric study. The goal of this study was to pick a baseline baffle spacing that would maximize the exergetic efficiency of studies involving only variable d_o, $\dot{m}_f$, and P_r, which affect the utilization more according to Figure 7. Figure 8 shows that the discharge exergetic efficiency initially is very low for small baffle spacings and asymptotically rises to a near steady value past a baffle spacing of 0.24 m. The same trend is seen for higher mass flow rates with exergetic efficiency becoming steady for baffle spacings of 0.24 m, 0.44 m, and 0.5 m for mass flow rates of 0.4 kg/s, 2.2

kg/s, and 3 kg/s, respectively. Exergetic efficiency was chosen to be steady when it varied less than 1% between tested baffle spacing values, and mass flow rates were evaluated in correspondence to desired discharge durations ranging between 3 hours and 16 hours which resemble desired discharge durations seen in CSP and CHP plants [9]. Low exergetic efficiency is observed for relatively low baffle spacing due to the high pressure drop within a system as dictated by Eq. 5. This high pressure drop results in a large amount of exergy destruction as visualized in Figure 8b. As baffle spacing increases, the exergy destruction within the system decreases and the exergetic efficiency asymptotically increases to a steady value. The exergy recovered also decreases due to the decreased shellside heat transfer coefficient within a system with fewer baffles, but this is seen to be at a much lesser rate than that of the decrease in exergy destruction. Due to the nonlinear decrease in pressure drop in comparison to the linear decrease of exergy recovered, a steady exergetic efficiency is reached. In order to maximize the exergetic efficiency within the system and conform to structural tube support standards set forth by the Tubular Exchanger Manufacturers Association (TEMA) [49], the baffle spacing was chosen to be fixed at 0.5 m for all mass flow rates and tube diameters considered.

With baffle spacing fixed at 0.5 m, the exergetic efficiency and utilization for a system with a fixed storage capacity of 4.5 MWh_t and air as the shellside HTF is considered here for study. Because of the fixed shell size, the storage capacity within the system will vary depending on the chosen tube diameter, tube pitch ratio, and HTF, as

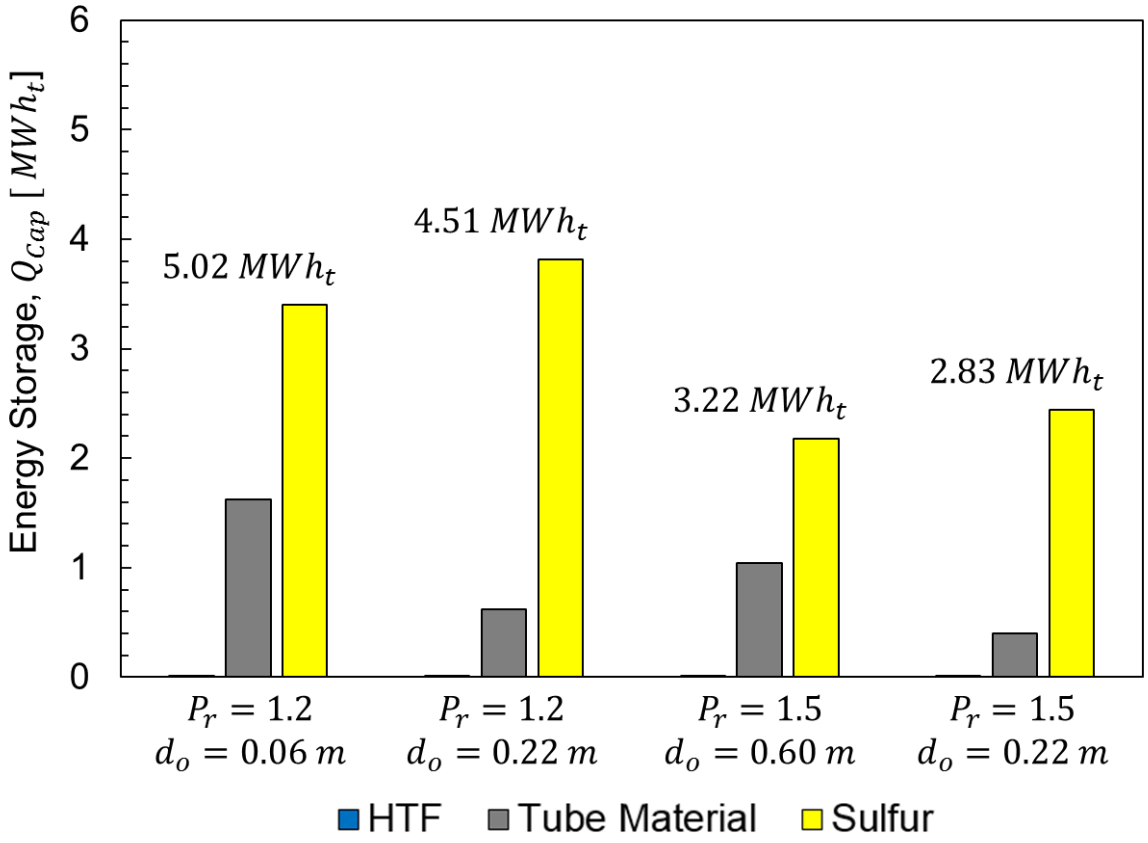

Figure 9: Variation in storage capacity of system based on tube pitch ratio and tube diameter using schedule 10 tubes. Overall storage capacity is shown above each column chart.

seen in Figure 9. In order to fix the storage capacity of systems with a variable tube diameter, the tube pitch ratio, P_r, was varied such that the rated capacity was constant. The resulting tube pitch ratio for each tube diameter is 1.2681, 1.2194, 1.2034, and 1.2000 for 0.06 m, 0.11 m, 0.17 m, and 0.22 m diameter tubes, respectively. Figure 10 shows plots of utilization, exergetic efficiency, and number of tubes by welded perimeter per utilized capacity, $\frac{N_t \times 2\pi d_o}{Q_{cap,u}}$, for systems with a variable tube diameter and mass flow rate during discharge. The utilization of energy vs mass flow rate is shown in Figure 10a. Utilization

is shown to decay with increasing mass flow rate and tube diameter for a number of reasons. As previously stated, an increased mass flow rate results in a decreased residence time of HTF within the system and higher stratification, leading to lower utilization. Furthermore, there is a decrease in performance for increasing tube diameter. This occurs because, for systems using larger diameter tubes, fewer tubes can be placed within a system with a fixed shell size, resulting in a lower surface area for convective

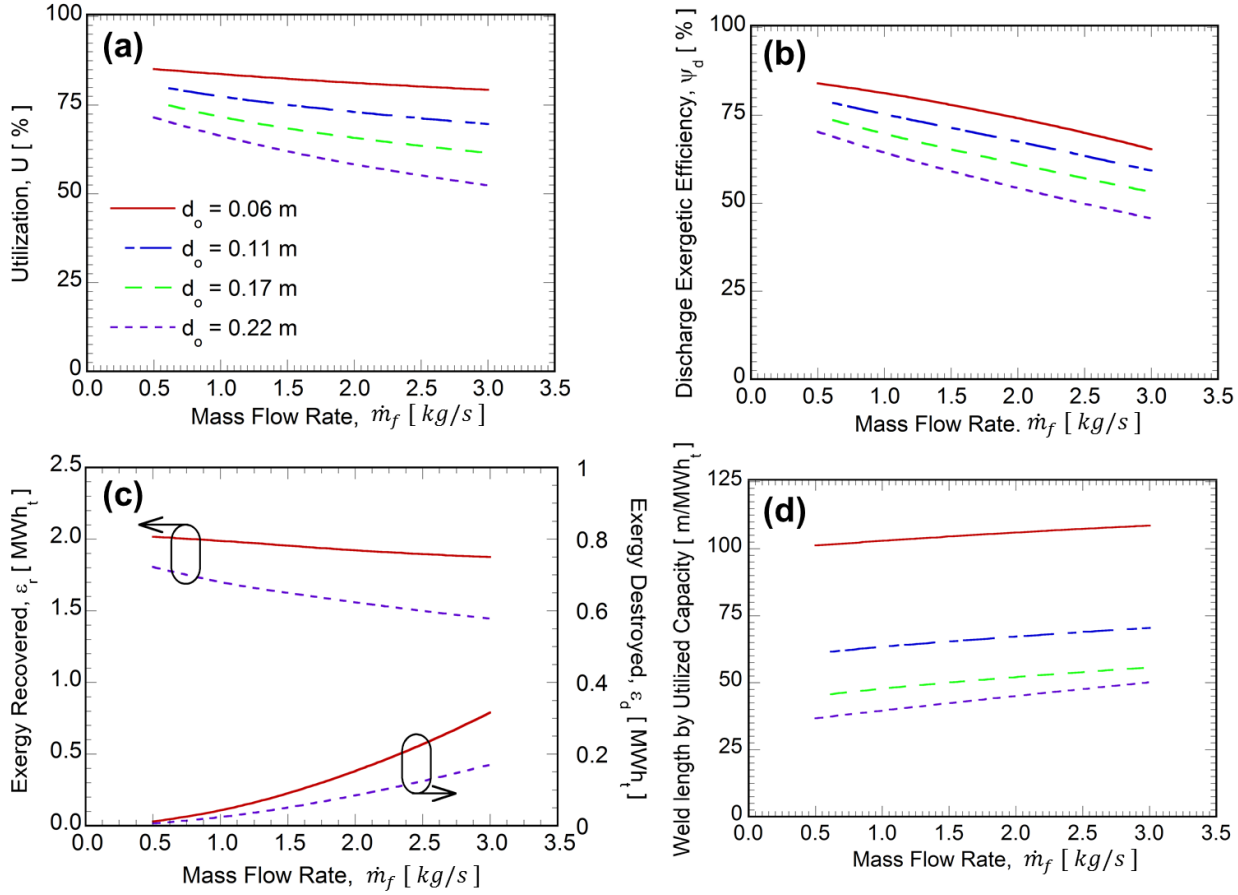

Figure 10: Effect of mass flow rate on (a) utilization, (b) exergetic efficiency, (c) exergy recovered and destroyed, and (d) weld length per utilized capacity for a 4.5 MWh_t fixed capacity storage system using air HTF.

heat transfer between the HTF and storage material (tube wall and sulfur). Additionally, larger diameter tubes result in lower tubeside convective heat transfer coefficient leading to further reduced heat transfer.

The variation of exergetic efficiency with mass flow rate is shown in Figure 10b. Similar to the utilization, the exergetic efficiency decays with mass flow rate with the efficiency being further reduced due to exergy destroyed from compressor work. As seen in Figure 10c, the exergy destroyed increases nonlinearly with mass flow rate, as a result of its relationship to pressure drop, resulting in decreased exergetic efficiency for higher flow rates. Similar decreases in exergetic efficiency are observed for larger tube diameters due to the decrease in exergy recovered caused by the increase in overall thermal resistance.

The welding costs play a dominating role in the total TES cost. They are typically estimated based on cost per length ($\frac{\$}{m\ of\ weld\ length}$), which necessitates the total weld length to be minimized for a cost-effective TES system. In lieu of a comprehensive economic model in this study, the total weld length per utilized capacity is computed as: $\ell_w = {N_t(2\pi d_o)}/{Q_{cap,u}}$. It is desirable for the total welding length, $N_t(2\pi d_o)$, to be minimized in order to reduce the welding cost, and for the utilized capacity, $Q_{cap,u}$, to be maximized in order to size the system correctly and recover the most thermal energy; for this reason, the best performance of $\ell_w$is one that is minimized. For this metric, ℓ_w, Figure

10d shows that the performance varies little for variable mass flow rate and improvement occurs via increase in the tube diameter. It is of note that there are diminishing returns on the reduction of ℓ_w with increasing d_o, with significant reduction being observed between $d_o = 0.06\,m$ to $d_o = 0.17\,m$ and minimal difference seen between $d_o = 0.17\,m$ and $d_o = 0.22\,m$. Hence, despite the lower performance in terms of exergetic efficiency, there is an interest in further investigating the cost of these systems.

A second study considered is that of a constant tube pitch ratio, P_r. For this study, the tube pitch ratio was maintained at either 1.2 or 1.5, and storage capacity was dictated by P_r and d_o as given by Figure 9. For shell and tube style heat exchangers, TEMA standards dictate that P_r should remain between 1.2 and 1.5, with values falling below this range creating difficulties in heat exchanger cleaning and maintenance, and values above this range leading to poor heat exchanger effectiveness [34]. Figure 7d shows that there is little variation in the final storage axial temperature profile and utilization between a system with $P_r = 1.2$ and $P_r = 1.5$, and thus, in an effort to limit the number of studies, these two tube pitch ratios are considered. Figure 11a and 10b show the discharge exergetic efficiency vs mass flow rate for $P_r = 1.2$ and $P_r = 1.5$. Just as in Figure 10b for the fixed capacity system, there is a decrease in exergetic efficiency with mass flow rate due to the corresponding increased exergy destruction, as seen in Figure 10c. This increased exergy destruction occurs due to the nonlinear dependence of pressure drop on mass flow rate (Eq. 8 – 11), and ultimately leads to the decrease in exergetic efficiency.

The difference in utilization shown in Figure 11c occurs for multiple reasons. As seen previously in Figure 9, the variation in P_r results in a decreased storage capacity. Additionally, increased P_r results in a fewer number of tubes within the system, decreased surface area for convective heat transfer, and lower crossflow Reynolds number, all of which are factors influencing the convective heat transfer and decreasing

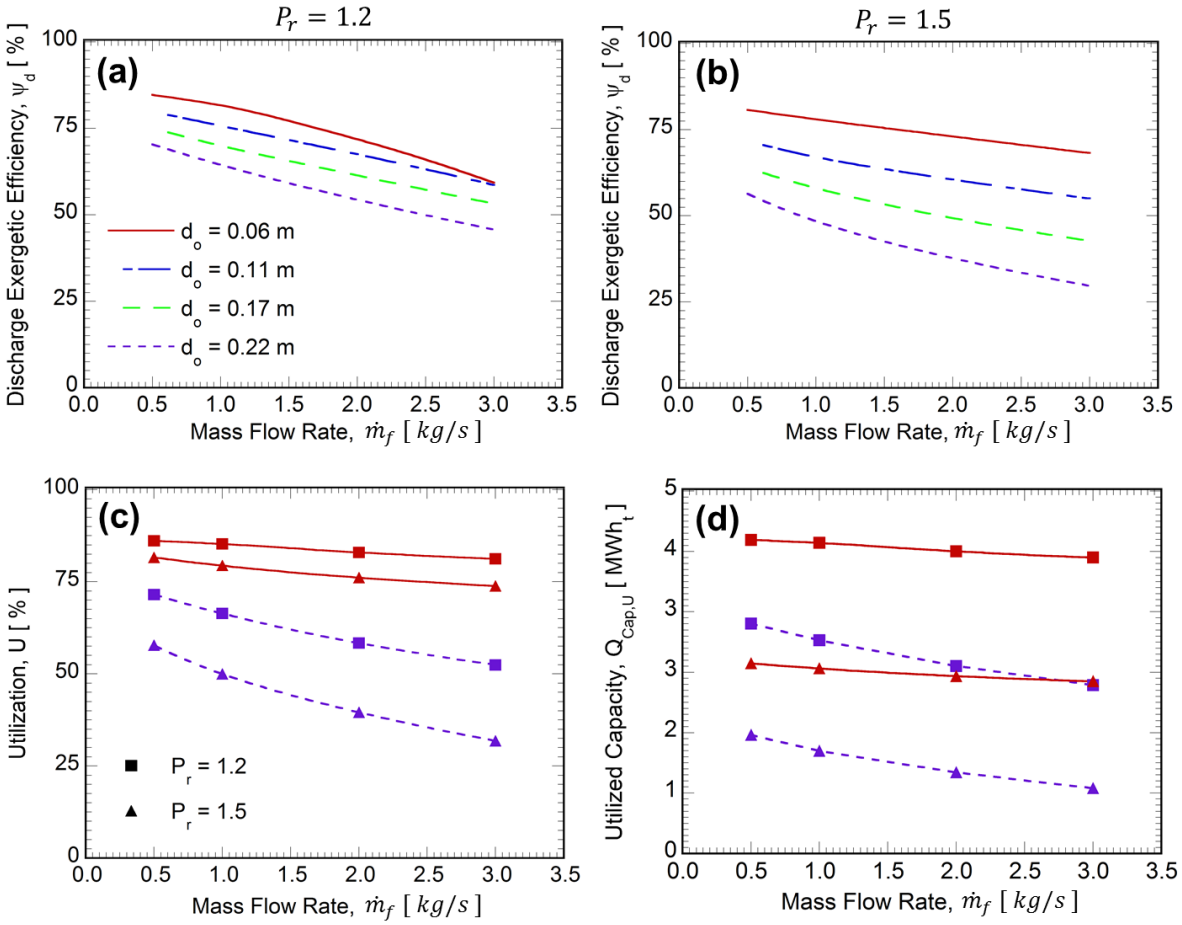

Figure 11: Effect of mass flow rate and tube diameter on the (a) exergetic efficiency for $P_r = 1.2$, (b) exergetic efficiency for $P_r = 1.5$, (c) Utilization of energy for $P_r = 1.2$ and $P_r = 1.5$, and (d) Utilized capacity for $P_r = 1.2$ and $P_r = 1.5$.

utilization. Due to the difference in tube pitch, nearly all utilized capacities (Figure 11d) from $P_r = 1.2$ are larger than that of utilized capacities of $P_r = 1.5$ with the exception of the case of $P_r = 1.2,\ d_o = 0.22\,m$ and $P_r = 1.5,\ d_o = 0.06\,m$; for this case, the latter configuration has a higher utilized capacity.

Figure 11a shows the influence of mass flow rate of air and storage tube diameter on total weld length per utilized capacity. It is observed that an increase in mass flow rate and pitch ratio increases ℓ_w due to a decrease in utilized capacity (Figure 11d). In general, an increase in tube diameter decreases ℓ_w due to decrease in number of tubes and weld length for a given storage capacity albeit the decrease in utilization (Figure 11c). However, for a mass flow rate of 3 kg/s and $P_r = 1.5$, it is seen that there is a preferred tube diameter at 0.17 m due to the competing effects of decrease in number of tubes and weld length, and decrease in energy utilization with increase in tube diameter.

In an effort to also account for the penalty associated with exergy loss in the system another metric — henceforth, known as the figure of merit (FOM) — $FOM = \frac{\ell_w}{\psi_d} = \frac{N_t(2\pi d_o)}{Q_{cap,u} \times \psi_d}$ is evaluated. Effectively, it provides a measure of the required length of tube welding for a system normalized to the quality of energy that can be delivered by the system during discharge. The system with the highest performance, according to the FOM, would be one that minimizes the amount of welding length to manufacture a system and maximizes the amount of high quality heat that can be delivered by a system. Thus, FOM should be minimized for the best performance. As can be seen in Figure 12b,

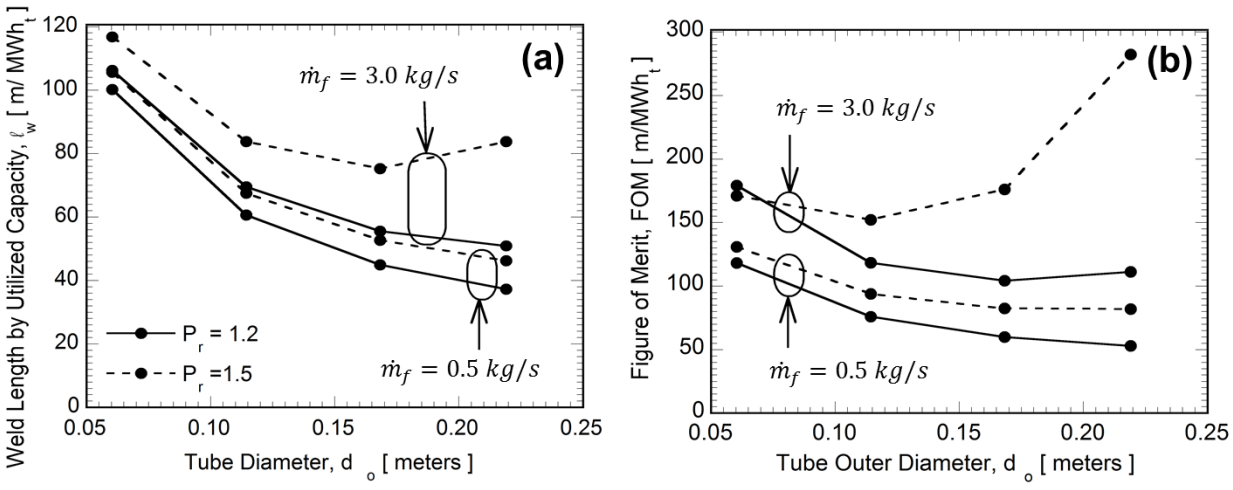

Figure 12: (a) Weld length by utilized capacity, $\ell_w = \frac{N_t(2\pi d_o)}{Q_{cap,u}}$, vs tube diameter, d_o, (b) figure of merit, $FOM = \frac{\ell_w}{\psi_d}$, vs tube outer diameter.

the contribution of exergetic efficiency for air HTF leads to more noticeable preferred design points for the parametric ranges considered than that of ℓ_w alone. With the added consideration of quality of heat delivered via inclusion of exergetic efficiency, Figure 12b shows that the preferred design point lies in the vicinity of $d_o = 0.17\ m$ (6″ NPS), for mass flow rates of $\dot{m}_f = 0.5\ kg/s$, and superior performance is exhibited for systems with lower tube pitch ratio. For mass flow rates of 3.0 kg/s the best design point lies in the vicinity of $d_o = 0.11\ m$ and $d_o = 0.17\ m$. The initial decrease in FOM occurs due to a large reduction in number of tube for welding from $d_o = 0.06\ m$ to $d_o = 0.11\ m$, resulting a lower welding perimeter despite the increase in tube diameter. The increase in FOM for larger d_o occurs due to decreases in exergetic efficiency, ψ_d, and utilization, U. Lower flow rates result in a less obvious design point, and there is little reduction in FOM past

$d_o = 0.17$ m. While the most ideal design for air lies in the vicinity of $d_o = 0.17$ m, there is a question of where the minimum of FOM lies, and optimization should be pursued in order to find the best design point.

Based on the studies performed here, a summary of the most preferred designs is given in Table 4 for the range of mass flow rate considered in this study. Overall, it shows that smaller tube diameter maximizes utilization and exergetic efficiency while larger tube diameter minimizes FOM, which captures the competing effects of required weld length and exergetic efficiency in a unified manner. As shown in Table 4a, utilization is shown to have a preferred design that occurs for the system of $P_r = 1.2$ and $d_o = 0.06\ m$ (2″ NPS) regardless of the mass flow rate. This is due to higher surface area for heat transfer interaction and high convective heat transfer coefficient allowing for increased recovery of stored energy during discharge. The design point based on maximizing exergetic efficiency (Table 4b) is shown to be variable of the mass flow rate. Low mass flow rates correspond to a preferred design point of $P_r = 1.2$ due to the increased amount of exergy stored within the system allowing for increased exergy recovery. However, due to the increased exergy destruction due to turbomachinery work at high flow rates, the preferred design point shifts to a system with $P_r = 1.5$ for $\dot{m}_f = 3.0\ kg/s$. From Table 4c, it is observed that minimum FOM is obtained at a different tube diameter design point from that of utilization and exergetic efficiency. Based on the competing effects of exergetic efficiency and utilization — which should be maximized — and total weld

Table 4: Preferred designs based on parametric studies

Objective	$\dot{m}_f \left[\frac{kg}{s}\right]$	U [%]	ψ [%]	$FOM \left[\frac{m}{MWh_t}\right]$	P_r	d_o [m]
a) Maximum Utilization, U						
	0.5	***86.09***	84.71	118.30	1.2	0.06 (2″NPS)
	3.0	***81.20***	59.25	104.34	1.2	0.06 (2″NPS)
b) Maximum Exergetic Efficiency						
	0.5	86.09	***84.71***	118.30	1.2	0.06 (2″NPS)
	3.0	73.86	***68.23***	171.16	1.5	0.06 (2″NPS)
c) Minimum FOM						
	0.5	76.24	75.08	***59.92***	1.2	0.17 (6″NPS)
	3.0	66.14	61.41	***104.34***	1.2	0.17 (6″NPS)

length of tubes in the system — which should be minimized— the preferred design point lies at $d_o = 0.17\ m$ (6″ NPS), regardless of the mass flow rate considered.

While the FOM provides a metric to compare welding costs to quality of heat delivered, there are methods that would improve the metric. By accounting for the overall cost of materials and manufacturing, a much more meaningful analysis could be obtained. By accounting for material cost, the effectively free cost of air can be weighed against that of other HTF. Additionally, the total manufacturing cost can account for the differing price per tube of different diameter tubes. Ultimately, this would better allow for comparison between systems with both different tube diameters and different tube pitch ratio, both parameter which affect the number of tubes within a system and cost.

Chapter 4: Conclusions

A verified, two dimensional, unsteady, numerical model of a high temperature sulfur-based shell and tube style storage system with the storage fluid on the tubeside was developed in this study for investigating the performance for variable mass flow rate, tube pitch, tube diameter, and baffle spacing. The performance of the systems was assessed based on the exergetic efficiency, energy utilization, and number of tubes by welded perimeter per utilized capacity. Based on the results a number of conclusions can be made as enumerated below:

- The performance metrics are shown to be most sensitive to tube diameter, tube pitch ratio, and mass flow rate.
- The highest energy utilizations are seen for tube diameters of 0.06 m (2″ NPS) and tube pitch ratios of 1.2, with a maximum energy utilization of 86.1% for the range of values considered.
- The maximum exergetic efficiency varies anywhere between 84.7% and 68.2% at the preferred design points. Exergy destruction due to compressor work has a considerable effect at elevated mass flow rates.
- Baffle spacing should be maintained at 50 cm (19.68″) for a standard 20′ intermodal container vessel in order to maintain high exergetic efficiency.
- Weld length per utilized capacity and FOM decrease with an increase in tube diameter due to a decrease in weld length, reach a minimum for tube diameter in

the vicinity of 0.17 m (6″ NPS), and increases again due to a decrease in utilization and exergetic efficiency.

- The weld length per utilized thermal capacity and FOM are valuable in assessing system performance, and can be made more valuable via inclusion of manufacturing and material costs.

References

[1] Zhang, H. L., Baeyens, J., Degrève, J., and Cacères, G., 2013, "Concentrated solar power plants: Review and design methodology," Renew. Sustain. Energy Rev., **22**, pp. 466–481.

[2] Flueckiger, S. M., Iverson, B. D., Garimella, S. V, and Pacheco, J. E., 2014, "System-level simulation of a solar power tower plant with thermocline thermal energy storage," Appl. Energy, **113**, pp. 86–96.

[3] Khan, K. H., Rasul, M. G., and Khan, M. M. K., 2004, "Energy conservation in buildings: Cogeneration and cogeneration coupled with thermal energy storage," Appl. Energy, **77**(1), pp. 15–34.

[4] Cárdenas, B., and León, N., 2013, "High temperature latent heat thermal energy storage: Phase change materials, design considerations and performance enhancement techniques," Renew. Sustain. Energy Rev., **27**, pp. 724–737.

[5] Lane, G. A., 1983, Solar Heat Storage: Latent Heat Materials, CRC Press, Boca Baton, Fla.

[6] Abedin, A., and Rosen, M., 2011, "A Critical Review of Thermochemical Energy Storage Systems.," Open Renew. Energy J., pp. 42–46.

[7] Cot-Gores, J., Castell, A., and Cabeza, L. F., 2012, "Thermochemical energy storage and conversion: A-state-of-the-art review of the experimental research under practical conditions," Renew. Sustain. Energy Rev., **16**(7), pp. 5207–5224.

[8] Stekli, J., Irwin, L., and Pitchumani, R., 2013, "Technical challenges and opportunities for concentrating solar power with thermal energy storage," J. Therm. Sci. Eng. Appl., **5**(2), p. 21011.

[9] DOE (US Department of Energy), 2012, Sunshot Vision Study.

[10] Laing, D., Steinmann, W.-D., Fiß, M., Tamme, R., Brand, T., and Bahl, C., 2008, "Solid Media Thermal Storage Development and Analysis of Modular Storage Operation Concepts for Parabolic Trough Power Plants," J. Sol. Energy Eng., **130**(February 2008), p. 11006.

[11] Nithyanandam, K., and Pitchumani, R., 2011, "Analysis and optimization of a latent thermal energy storage system with embedded heat pipes," Int. J. Heat Mass Transf., **54**(21–22), pp. 4596–4610.

[12] Tian, Y., and Zhao, C. Y., 2013, "A review of solar collectors and thermal energy storage in solar thermal applications," Appl. Energy, **104**, pp. 538–553.

[13] Clark, P. D., and Dowling, N. I., 2004, "Capture of Solar Energy Using Elemental Sulfur," J. Sulfur Chem., **25**(1), pp. 7–11.

[14] Rau, H., Kutty, T. R. N., and Guedes de Carvalho, J. R. F., 1973, "High temperature saturated vapour pressure of sulphur and the estimation of its critical quantities," J. Chem. Thermodyn., **5**(2), pp. 291–302.

[15] "Personal Communication, California Sulfur Company, August 2016."

[16] Wentworth, W. E., and Chen, E., 1976, "Simple thermal decomposition reactions

for storage of solar thermal energy," Sol. Energy, **18**(3), pp. 205–214.

[17] Wong, B., Roeb, M., Thomey, D., Buckingham, R., Brown, L., and Sattler, C., 2014, "Sulfur Based Thermochemical Energy Storage for Concentrated Solar Power," Proceeding of the ASME 2013 7th Inernational Conference on Energy Sustainability, pp. 7–12.

[18] Lacroix, M., 1993, "Numerical simulation of a shell-and-tube latent heat thermal energy storage unit," Sol. Energy, **50**(4), pp. 357–367.

[19] He, Q., and Zhang, W. N., 2000, "a Study on Latent Heat Storage Exchangers With the High Temperature Pcm," World Renew. Energy Congr. VI, (January 2000), pp. 1044–1047.

[20] Trp, A., 2005, "An experimental and numerical investigation of heat transfer during technical grade paraffin melting and solidification in a shell-and-tube latent thermal energy storage unit," Sol. Energy, **79**(6), pp. 648–660.

[21] Ganapathi, G. B., Bame, D., Furst, B., Angeles, L., and Pauken, M., 2013, "A 5KWht lab-scale demonstration of a novel thermal energy storage concept with supercritical fluids," pp. 1–9.

[22] Tse, L. A., Lavine, A. S., Lakeh, R. B., and Wirz, R. E., 2015, "Exergetic optimization and performance evaluation of multi-phase thermal energy storage systems," Sol. Energy, **122**, pp. 396–408.

[23] Barton, N. G., 2013, "Simulations of air-blown thermal storage in a rock bed,"

Appl. Therm. Eng., **55**(1–2), pp. 43–50.

[24] Hänchen, M., Brückner, S., and Steinfeld, A., 2011, "High-temperature thermal storage using a packed bed of rocks e Heat transfer analysis and experimental validation," Appl. Therm. Eng., **31**(10), pp. 1798–1806.

[25] Mertens, N., Alobaid, F., Frigge, L., and Epple, B., 2014, "Dynamic simulation of integrated rock-bed thermocline storage for concentrated solar power," Sol. Energy, **110**, pp. 830–842.

[26] Chandra, P., and Willits, D. H., 1981, "Pressure drop and heat transfer characteristics of air-rockbed thermal storage systems," Sol. Energy, **27**(6), pp. 547–553.

[27] Avila-Marin, A. L., 2011, "Volumetric receivers in Solar Thermal Power Plants with Central Receiver System technology: A review," Sol. Energy, **85**(5), pp. 891–910.

[28] International Organization for Standardization, 2013, ISO 668:2013 Series 1 Freight Containers - Classifications, Dimensions, and Ratings - Ammendment 1.

[29] Nithyanandam, K., Barde, A., and Wirz, R. E., 2016, "Charge- and discharge characteristics of elemental sulfur in horizontal tubes for high temperature thermal energy storage," Appl. Energy.

[30] The American Society of Mechanical Engineers, 2015, Welded and Seamless Wrought Steel Pipe, The American Society of Mechanical Engineers, New York.

[31] Kern, D. Q., 1990, Process Heat Transfer, McGraw-Hill.

[32] Bell, K., 1963, Final report of the cooperative research program on shell-and-tube heat exchangers.

[33] Wills, M. J. N., and Johnson, D., 1984, "A New and Accurate Hand Calculation method for Shell-Side Pressure Drop and Flow Distribution," 22nd Nat. Heat Transfer Conf. ASME, New York.

[34] Bell, K., Chisholm, D., and Cooper, A., 1983, Heat Exchanger Design Handbook, Hemisphere Publishing Corporation.

[35] Taborek, J., 1988, "Shell-and-tube heat exchangers," Heat Exchanger Design Handbook, Vol. 3., Hemisphere Publishing Corporation, New York.

[36] Bergman, T. L., Lavine, A. S., Incropera, F. P., and Dewitt, D. P., 2011, Fundamentals of Heat and Mass Transfer, John Wiley & Sons.

[37] Serrano-lópez, R., Fradera, J., and Cuesta-lópez, S., 2013, "Molten salts database for energy applications."

[38] Moran, M. J., Shapiro, H. N., Boettner, D. D., and Bailey, M. B., 2011, Fundamentals of Engineering Thermodynamics, John Wiley & Sons.

[39] Patankar, S. V., 1980, Numerical Heat Transfer and Fluid Flow.

[40] Jegadheeswaran, S., Pohekar, S. D., and Kousksou, T., 2010, "Exergy based performance evaluation of latent heat thermal storage system: A review," Renew. Sustain. Energy Rev., **14**(9), pp. 2580–2595.

[41] Kaizawa, A., Kamano, H., Kawai, A., Jozuka, T., Senda, T., Maruoka, N., and Akiyama, T., 2008, "Thermal and flow behaviors in heat transportation container using phase change material," Energy Convers. Manag., **49**(4), pp. 698–706.

[42] Rosen, M. A., 1992, "Appropriate Thermodynamic Performance Measures for Closed Systems for Thermal Energy Storage," **114**(May).

[43] Erek, A., and Dincer, I., 2009, "A New Approach to Energy and Exergy Analyses of Latent Heat Storage Unit," Heat Transf. Eng., **30**(6), pp. 506–515.

[44] Watanabe, T., and Kanzawa, A., 1995, "Second law optimization of a latent heat storage system with PCMS having different melting points," Heat Recover. Syst. CHP, **15**(7), pp. 641–653.

[45] Riaz, M., 1977, "Analytical Solutions for Single and Two-Phase Models of Packed-Bed Thermal Storage Systems," J. Heat Transfer, **99**(August), pp. 489–492.

[46] Lew, J. T. Van, Li, P., and Stephens, J., 2011, "Analysis of Heat Storage and Delivery of a Thermocline Tank," **133**(May 2011), pp. 1–10.

[47] Yang, Z., and Garimella, S. V, 2010, "Thermal analysis of solar thermal energy storage in a molten-salt thermocline," Sol. Energy, **84**(6), pp. 974–985.

[48] Kakac, S., and Liu, H., 2002, Heat Exchangers: Selection, Rating, and Thermal Design, CRC Press.

[49] Tubular Exchanger Manufacturers Association Inc., 1999, Standards of the Tubular Exchanger Manufacturers Asscociation, Tarrytown, NY.